

Discovery of a directly imaged disk in scattered light around the Sco-Cen member Wray 15-788[★]

A. J. Bohn¹, M. A. Kenworthy¹, C. Ginski^{1,2}, M. Benisty^{3,4}, J. de Boer¹, C. U. Keller¹, E. E. Mamajek^{5,6}, T. Meshkat⁷, G. A. Muro-Arena², M. J. Pecaut⁸, F. Snik¹, S. G. Wolff¹, and M. Reggiani^{9,10}

¹ Leiden Observatory, Leiden University, PO Box 9513, 2300 RA Leiden, The Netherlands
e-mail: bohn@strw.leidenuniv.nl

² Sterrenkundig Instituut Anton Pannekoek, Science Park 904, 1098 XH Amsterdam, The Netherlands

³ Unidad Mixta Internacional Franco-Chilena de Astronomía (CNRS, UMI 3386), Departamento de Astronomía, Universidad de Chile, Camino El Observatorio 1515, Las Condes, Santiago, Chile

⁴ Univ. Grenoble Alpes, CNRS, IPAG, 38000 Grenoble, France.

⁵ Jet Propulsion Laboratory, California Institute of Technology, 4800 Oak Grove Drive, M/S 321-100, Pasadena, CA, 91109, USA

⁶ Department of Physics & Astronomy, University of Rochester, Rochester, NY 14627, USA

⁷ IPAC, California Institute of Technology, M/C 100-22, 1200 East California Boulevard, Pasadena, CA 91125, USA

⁸ Rockhurst University, Department of Physics, 1100 Rockhurst Road, Kansas City, MO 64110, USA

⁹ Space sciences, Technologies and Astrophysics Research (STAR) Institute, Université de Liège, Allée du 6 Août 17, Bat. B5C, 4000 Liège, Belgium

¹⁰ Institute of Astronomy, KU Leuven, Celestijnenlaan 200D, B-3001 Leuven, Belgium

Received October 28, 2018 / Accepted February 20, 2019

ABSTRACT

Context. Protoplanetary disks are the birth environments of planetary systems. Therefore, the study of young, circumstellar environments is essential to understand the processes taking place in planet formation and the evolution of planetary systems.

Aims. We aim to detect and characterize circumstellar disks and potential companions around solar-type, pre-main-sequence stars in the Scorpius-Centaurus Association (Sco-Cen).

Methods. As part of our on-going survey we have carried out high-contrast imaging with VLT/SPHERE/IRDIS to obtain polarized and total intensity images of the young (11⁺¹⁶₋₇ Myr old) K3IV star Wray 15-788 within the Lower Centaurus Crux subgroup of Sco-Cen. For the total intensity images, we remove the stellar halo by an approach based on reference star differential imaging in combination with principal component analysis.

Results. Both total intensity and polarimetric data resolve a disk around the young, solar-like Sco-Cen member Wray 15-788. Modeling of the stellar spectral energy distribution suggests that this is protoplanetary disk at a transition stage. We detect a bright, outer ring at a projected separation of ~ 370 mas (≈ 56 au), hints for inner substructures at ~ 170 mas (≈ 28 au) and a gap in between. Only within a position angle range of $60^\circ < \phi < 240^\circ$, we are confident at 5σ level to detect actual scattered light flux from the outer ring of the disk; the remaining part is indistinguishable from background noise. For the detected part of the outer ring we determine a disk inclination of $i = 21^\circ \pm 6^\circ$ and a position angle of $\varphi = 76^\circ \pm 16^\circ$. Furthermore, we find that Wray 15-788 is part of a binary system with the A2V star HD 98363 at a separation of $\sim 50''$ (≈ 6900 au).

Conclusions. The detection of only half of the outer ring might be due to shadowing by a misaligned inner disk. A potential substellar companion can cause the misalignment of the inner structures and can be responsible for clearing the detected gap from scattering material. We can not, however, rule out the possibility of a non-detection due to our limited signal to noise ratio, combined with brightness azimuthal asymmetry. From our data, we can exclude companions more massive than $10 M_{\text{Jup}}$ within the gap at a separation of ~ 230 mas (≈ 35 au). Additional data are required to characterize the disk's peculiar morphology and to set tighter constraints on the potential perturber's orbital parameters and mass.

Key words. protoplanetary disks – planets and satellites: formation – planet-disk interactions – techniques: image processing – stars: individual: Wray 15-788, HD 98363

1. Introduction

In the past few years, the second generation of high-contrast imaging instruments such as the Spectro-Polarimetric High-contrast Exoplanet REsearch (SPHERE, Beuzit et al. 2008) instrument and the Gemini Planet Imager (GPI, Macintosh et al. 2006) have resolved and characterized several disks around

young, pre-main sequence stars (e.g., Avenhaus et al. 2018; Millar-Blanchaer et al. 2017). These range from warm, gas-rich protoplanetary disks around young, stars of ages usually lower than 10 Myr (Andrews et al. 2012) to cold debris disks around more evolved stars, where the primordial gas has already dissipated (Matsuyama et al. 2003; Wyatt et al. 2003). Since planets form within protoplanetary disks (Goldreich & Ward 1973), the characterization of circumstellar environments and the search for planetary mass companions is closely related. The study of

[★] Based on observations collected at the European Organisation for Astronomical Research in the Southern Hemisphere under ESO programmes 099.C-0698(A), 0101.C-0153(A) and 0101.C-0464(A).

young stellar systems, therefore, gives us an understanding of the initial conditions of planet formation.

With a mean distance of ~ 130 pc (de Zeeuw et al. 1999) and an average age of 14 ± 3 Myr (Pecaut & Mamajek 2016), the Scorpius-Centaurus Association (Sco-Cen, de Zeeuw et al. 1999) is one of the closest sites of recent star formation to the Sun. Therefore, Sco-Cen is an ideal region, when it comes to the search for young, luminous planets or protoplanetary and early debris disks. Pecaut & Mamajek (2016) identified and characterized 156 new K-type star members of Sco-Cen. One object in this sample is the emission-line star Wray 15-788 (2MASS J11175186-6402056, Hen 3-632), which is located in the Lower Centaurus-Crux (LCC) subgroup of Sco-Cen (Mamajek et al. 2013; Pecaut & Mamajek 2016). It was discovered as an $H\alpha$ emission object by Wray (1966) and confirmed within the study of southern emission line stars by Henize (1976). The star is of spectral type K3IVe, has a mass of $1.2 M_{\odot}$ (Pecaut & Mamajek 2016), and a distance of 139.7 ± 0.5 pc (Gaia Collaboration et al. 2018). In addition, Pecaut & Mamajek (2016) determined an age of 4 Myr, which is likely an underestimate. A more accurate age may be obtained by using evolutionary models that include magnetic fields (Feiden 2016) as presented in Sect. 5.1 of this work. Table 1 summarizes the most important stellar parameters of Wray 15-788.

In Sect. 2 we describe the SPHERE data we obtained on Wray 15-788 and Sect. 3 explains our applied data reduction techniques. Thereafter, we present our observational results in Sect. 4 and an analysis of these data is given in Sect. 5. Furthermore, we show the association of Wray 15-788 as a comoving companion to the main sequence star HD 98363 and derive new estimates for ages and masses of both objects. A model of the stellar spectral energy distribution (SED) is also presented in Sect. 5. Eventually, we discuss our results in Sect. 6 and present the conclusions of the article in Sect. 7.

2. Observations

All our observations are performed with SPHERE, which is mounted on the Naysmith platform of Unit 3 telescope (UT3) at ESO's VLT. To obtain almost diffraction limited data, SPHERE is assisted by the SAXO extreme adaptive optics system (Fusco et al. 2006; Petit et al. 2014). In particular, we made use of the infrared dual-band imager and spectrograph (IRDIS, Dohlen et al. 2008), which was operated in both dual-polarization imaging (DPI, Langlois et al. 2014) and classical imaging (CI, Vigan et al. 2010) modes to obtain high-contrast polarized and total intensity images of the system. A detailed description of the observations is presented in Table 2.

2.1. Classical imaging

The CI observations (PI: M. A. Kenworthy) were obtained on May 14, 2018, within a larger program looking for planetary mass companions around solar-type stars in Sco-Cen (Bohn et al. in prep). The target was observed in good weather conditions with two broadband filters in H - and K_s -band (Filter IDs: BB_H, BB_Ks) for 128 s each. The central wavelengths of the filters are $\lambda_c^H = 1625.5$ nm and $\lambda_c^{K_s} = 2181.3$ nm with bandwidths of $\Delta\lambda^H = 291.0$ nm and $\Delta\lambda^{K_s} = 313.5$ nm, respectively. To reduce the effect of bad detector pixels, a dither pattern on a 2×2 grid with 1 pixel spacing is applied during the observation. Additionally, an apodized pupil Lyot coronagraph (Soummer 2005; Carillet et al. 2011; Guerri et al. 2011) with a diameter of 185 mas (Coro-

nagraph ID: N_ALC_YJH_S) was used to block the central flux of the star. The observations were carried out in pupil-stabilized mode, but the amount of field rotation during the observation was less than 1° . To model the thermal sky and instrument background, an additional exposure with the science setup was taken at an offset sky position without any source. Center frames were obtained, for which a sinusoidal pattern was applied to the deformable mirror in order to create four calibration spots around the target's position behind the coronagraphic mask. In addition, we obtained unsaturated, non-coronagraphic flux frames of the star with a neutral density filter (Filter ID: ND_1.0) in place to avoid saturation of the detector.

2.2. Dual-polarization imaging

The DPI observation (PI: M. Benisty) was carried out on the night of June 5, 2018, under very poor weather conditions. We obtained one polarimetric cycle, which consists of one image for each of the four half-wave plate positions (0° , 45° , 22.5° , and 67.5°) with an exposure time of 64 s each. Furthermore, we applied the same coronagraph and broadband filter in H -band as used for the CI observations. In a similar manner as described before, we also obtained additional center and sky frames for the DPI observation. The DPI cycle was conducted in field-stabilized mode.

3. Data reduction

Both CI and DPI data are reduced by a personal processing pipeline based on the new release of the PynPoint package (Stolker et al. 2019). This includes basic image processing steps such as flat fielding and sky subtraction for both CI and DPI data. Furthermore, a simple bad pixel correction is applied by a 5σ box filtering algorithm (based on the IDL routine of Varosi & Gezari 1993).

3.1. Classical imaging

The dithering offsets of the science images to the center frame are registered and all frames are aligned accordingly. Afterwards, the aligned science images are centered with respect to the star's position behind the coronagraph. This position is determined as the center of the four calibration spots within the additionally obtained center frame (see Langlois et al. 2013). Because IRDIS is operated in CI mode, we obtain two copies of the coronagraphic stellar point spread function (PSF) simultaneously for each exposure (see Dohlen et al. 2008). To compensate for bad pixel introduced noise, we average the two centered PSFs from both detector sides for each individual exposure. Finally, we remove the stellar halo and instrumental artifacts by an approach based on reference star differential imaging (RDI, Smith & Terrile 1984; Lafrenière et al. 2007). Within a larger survey for planets around solar-type stars (PI: M. A. Kenworthy) in Sco-Cen, we observed 26 and 12 stars in H - and K_s -band, respectively. A detailed list of these reference stars and the observing conditions is presented in Appendix A. The stars are very similar to Wray 15-788 in terms of spectral type, mass, age, distance, position on sky, and apparent magnitude. Furthermore, they were observed with exactly the same observational setup as Wray 15-788. Therefore, we create a library from these reference targets, which we analyze with regard to its principal components (principal components analysis: PCA, Amara & Quanz 2012; Soummer et al. 2012). Thereafter, the

Table 1. Stellar parameters of Wray 15-788 and HD 98363.

| Parameter | Value | | Reference(s) |
|----------------------------|------------------------|-------------------------|--------------|
| | Wray 15-788 | HD 98363 | |
| Right ascension (J2000) | 11:17:51.87 | 11:17:58.14 | (1) |
| Declination (J2000) | -64:02:05.60 | -64:02:33.35 | (1) |
| Spectral Type | K3IVe | A2V | (2,3) |
| Mass [M_{\odot}] | $1.26^{+0.07}_{-0.22}$ | $1.92^{+0.08}_{-0.08}$ | (2,4) |
| Effective Temperature [K] | $4\,549^{+225}_{-215}$ | $8\,830^{+331}_{-319}$ | (2,4) |
| Luminosity [L_{\odot}] | $0.91^{+0.07}_{-0.06}$ | $14.96^{+1.44}_{-1.32}$ | (2,4) |
| Age ^a [Myr] | 11^{+16}_{-7} | 11^{+16}_{-7} | (2,4) |
| Parallax [mas] | 7.159 ± 0.027 | 7.215 ± 0.034 | (1) |
| Distance [pc] | 139.126 ± 0.52 | 138.044 ± 0.66 | (1,5) |
| Proper motion (RA) [mas] | -28.583 ± 0.042 | -28.491 ± 0.053 | (1) |
| Proper motion (Dec) [mas] | -1.411 ± 0.040 | -0.795 ± 0.051 | (1) |
| V [mag] | 11.89 ± 0.08 | 7.85 ± 0.01 | (2,6,7) |
| B – V [mag] | 1.11 ± 0.09 | 0.18 ± 0.01 | (2,6,7) |
| J [mag] | 9.39 ± 0.02 | 7.53 ± 0.02 | (2,8) |
| H [mag] | 8.59 ± 0.04 | 7.48 ± 0.03 | (2,8) |
| K_s [mag] | 8.18 ± 0.03 | 7.50 ± 0.02 | (2,8) |
| W1 [mag] | 7.75 ± 0.02 | 7.36 ± 0.03 | (2,9) |
| W2 [mag] | 7.49 ± 0.02 | 7.43 ± 0.02 | (2,9) |
| W3 [mag] | 6.42 ± 0.02 | 6.93 ± 0.02 | (2,9) |
| W4 [mag] | 3.88 ± 0.02 | 4.64 ± 0.02 | (2,9) |

Notes. ^(a) The primary, HD 98363, has a most likely age of 11 Myr, but since the error bars of the primary overlap the main sequence in the Hertzsprung-Russell diagram, the 95% confidence range of 22 Myr to 480 Myr does not contain the mode. Given its membership in Sco-Cen, this is not a useful age constraint. The secondary, Wray 15-788, is in a stage of evolution where we can place meaningful limits on the age, so we adopt the system age as that of the secondary, 11 Myr with 95% CL range of 11^{+16}_{-7} Myr.

References. (1) Gaia Collaboration et al. (2018); (2) Pecaut & Mamajek (2016); (3) Houk & Cowley (1975); (4) Sect. 5.1 of this work; (5) Bailer-Jones et al. (2018); (6) Henden et al. (2012); (7) Høg et al. (2000); (8) Cutri et al. (2012a); (9) Cutri et al. (2012b)

Table 2. Observations of Wray 15-788 carried out with SPHERE/IRDIS.

| Observation date (yyyy-mm-dd) | Mode ^a | Filter | NDIT×DIT ^b (1×s) | $\Delta\pi^c$ (°) | $\langle\omega\rangle^d$ (") | $\langle X\rangle^e$ | $\langle\tau_0\rangle^f$ (ms) |
|----------------------------------|-------------------|--------|--------------------------------|----------------------|---------------------------------|----------------------|----------------------------------|
| 2018-05-14 | CI | H | 4×32 | 0.86 | 0.86 | 1.30 | 2.55 |
| 2018-05-14 | CI | K_s | 4×32 | 0.87 | 0.85 | 1.30 | 2.15 |
| 2018-06-05 | DPI | H | 4×64 | - | 0.99 | 1.30 | 1.48 |

Notes. ^(a) Observation mode is either classical imaging (CI) or dual-polarization imaging (DPI). ^(b) NDIT describes the number of dithering positions and DIT is the detector integration time per dithering position. ^(c) $\Delta\pi$ describes the amount of field rotation during the observation, if it is carried out in pupil-stabilized mode (only valid for CI observations). ^(d) $\langle\omega\rangle$ denotes the average seeing conditions during the observation. ^(e) $\langle X\rangle$ denotes the average airmass during the observation. ^(f) $\langle\tau_0\rangle$ denotes the average coherence time during the observation.

PSF of Wray 15-788 in each science frame is modeled as linear combination of the first m principal components (PCs) from the reference library (RDI+PCA, e.g., Choquet et al. 2014). These PSF-models are subtracted from the science images, the residuals are de-rotated according to their parallactic angle and median combined. For characterization of disks at low inclination, this technique has proven superior compared to algorithms based on angular differential imaging (Marois et al. 2006), which leads to undesirable self-subtraction effects from radial symmetric parts of the disk (Choquet et al. 2014). An additional constant rotation of 135°99 in counterclockwise direction is applied to correct for the instrument’s offset angle included to align the pupil

with the Lyot stop¹. We used the general astrometric solution for IRDIS with a plate scale of 12.251 ± 0.009 mas per pixel and 12.265 ± 0.009 mas per pixel for H- and K_s -band, respectively, as well as a true north correction of $-1^{\circ}75 \pm 0^{\circ}08$ according to Maire et al. (2016).

3.2. Dual-polarization imaging

The reduction of the DPI data was carried out analogously to the description given in Ginski et al. (2016).

¹ This value is obtained from the latest version of the instrument manual: <https://www.eso.org/sci/facilities/paranal/instruments/sphere/doc.html>

4. Observational results

The results of our data reduction are presented in Fig. 1. For both CI and DPI, an artificial mask with a diameter of ~ 196 mas is applied to hide the innermost parts of the images that are obscured by the coronagraphic mask and polluted by leaking flux around it. Furthermore, each pixel is scaled by the squared, de-projected radial separation to the image center, to account for intensity loss in scattered light and to highlight features of the disk. For a correct deprojection we use an inclination of 21° and a position angle of 76° according to our disk fitting results presented in Sect. 5.3.1.

4.1. CI data

In frame **a** and **b** of Fig. 1 we present the SPHERE/CI results in H - and K_s -band, respectively. We model the stellar PSFs with 20 PCs² from our reference library and subtract these models afterwards. A bright disk that shows several features is detected in both filters. Most prominent are:

- (i) *Ring A*: A bright outer arc at an average projected separation of ~ 370 mas that is brightest southeast of the star and indistinguishable from background noise in the northwest.
- (ii) *Ring B*: A tentative, circular inner ring at an average projected separation of ~ 170 mas.
- (iii) A gap in between both rings.

An annotated image of the disk, in which the main features are highlighted, is presented in Fig. 2. All these detected features of the disk are analyzed in depth within Sect. 5.3 and discussed within Sect. 6.

4.2. DPI data

In frames **c** and **d** of Fig. 1 we present Stokes Q and U parameters of the SPHERE/DPI data. To increase signal to noise in the poor quality observations, we smooth the images with a Gaussian kernel that has a full width at half maximum (FWHM) of ~ 50 mas. This corresponds to the diffraction limited size of the SPHERE PSF in H -band. Both polarimetric results reveal a strong butterfly-like pattern, approximately centered at the star's position behind the coronagraph. This agrees with what we expect of azimuthal linear polarization of light scattered by a circumstellar disk. The positive flux extends down to the artificial mask that we have applied in the image center. However, this does not necessarily mean that we receive scattered light flux from all separations down to the mask's radial separation of ~ 98 mas, due to the poor weather conditions and the previously performed smoothing. Furthermore, an excess of flux in the southeastern part compared to the northwestern part of the disk is detected in both Q and U images, which agrees very well with the shape of *ring A* that we detect in the CI results. Moreover, the scattered light flux in the DPI result seems to extend farther out compared to the distinct shape of *ring A* in the CI results. Whether this extended structure is real or just caused by the applied smoothing and due to the poor weather conditions during the observation, will be analyzed in Sect. 5.3.1.

² We optimized the number of fitted principal components in order to achieve the best contrast inside the possible disk gap at a projected separation of ~ 220 mas.

5. Analysis

5.1. Association of Wray 15-788 with HD 98363

In our investigation we discovered that Wray 15-788 is part of a multiple system with the A2V star HD 98363 (HIP 55188). HD 98363 is a main sequence star of spectral type A2V (Houk & Cowley 1975) and de Zeeuw et al. (1999) had identified it as a member of LCC based on Hipparcos astrometry. Tetzlaff et al. (2011) estimated an isochronal age of 13.0 ± 3.7 Myr to HD 98363 and constrained a mass of $2.0 \pm 0.1 M_\odot$. Considering binarity with Wray-15-788, we aim to derive new estimates for these parameters. All important stellar properties are listed in Table 1.

Our companionship analysis is based on parallaxes and proper motions from Gaia DR2 (ICRS, epoch 2015.5, Gaia Collaboration et al. 2018), which are listed in Table 1 as well. The calculated separation of the binary is $49''.64974 \pm 0.05$ mas and the distances agree within 1.08 ± 0.84 parsecs, statistically consistent with these two stars being co-distant. The differential velocity in the plane of the sky between the two stars is 0.623 ± 0.462 mas/year. An estimate of the orbital period of the binary with a separation of 6900 au is around 330 kyr, with a circular orbital velocity of 0.63 km/s, which is 0.001 mas/year. This is marginally consistent with the differential velocity of the two stars above. So, Wray 15-788 is actually HD 98363 B: a stellar companion to HD 98363.

Furthermore, Chen et al. (2012) detect a debris disk around HD 98363 based on $24 \mu\text{m}$ and $70 \mu\text{m}$ photometry from *Spitzer* MIPS (Werner et al. 2004; Rieke et al. 2004). Moór et al. (2017) report a non-detection of CO with an upper limit of 0.036 Jy km/s on the integrated line flux of ^{12}CO J=2–1. This gas-poor debris disk around HD 98363 is especially interesting due to our finding of a disk around Wray 15-788. A discussion of this special binary system with two hosts of circumstellar disks is presented in Sect. 6.3.

To derive consistent masses and ages of the binary system we analyze both stars within an Hertzsprung-Russell diagram as presented in Fig. 3. We estimate both masses and ages using Feiden/Dartmouth tracks (Feiden 2016). These models include magnetism below $1.7 M_\odot$ and yield a consistent age for the Upper Scorpius subgroup of Sco-Cen (Feiden 2016). Therefore, they define a good basis for an analysis of our two LCC objects. Using a flat age and Maschberger (2013) initial mass function as priors, we obtain masses of $1.26^{+0.07}_{-0.22} M_\odot$ and $1.92^{+0.08}_{-0.08} M_\odot$ for Wray 15-788 and HD 98363, respectively. Furthermore, we obtain an age of 11^{+16}_{-7} Myr for both companions, apparent in Fig. 3.

5.2. SED modeling

We obtain the available SED of Wray 15-788 as presented in Fig. 4. Whereas it is rather well sampled by *APASS* (Henden & Munari 2014), *Gaia* (Gaia Collaboration et al. 2018), *2MASS* (Cutri et al. 2012a), and *DENIS* (Epchtein et al. 1997) photometry for wavelengths up to approximately $2 \mu\text{m}$, we only have a few datapoints from *WISE* (Cutri et al. 2012b), *IRAS* (Neugebauer et al. 1984), *AKARI/FIS* (Murakami et al. 2007; Kawada et al. 2007), *AKARI/IRC* (Murakami et al. 2007; Ishihara et al. 2010), and additional upper limits from *IRAS* for wavelengths longer than this. Especially, there is no data available beyond $160 \mu\text{m}$.

To evaluate whether the system is a potential gas-rich protoplanetary disk, we aim to derive the fractional infrared luminos-

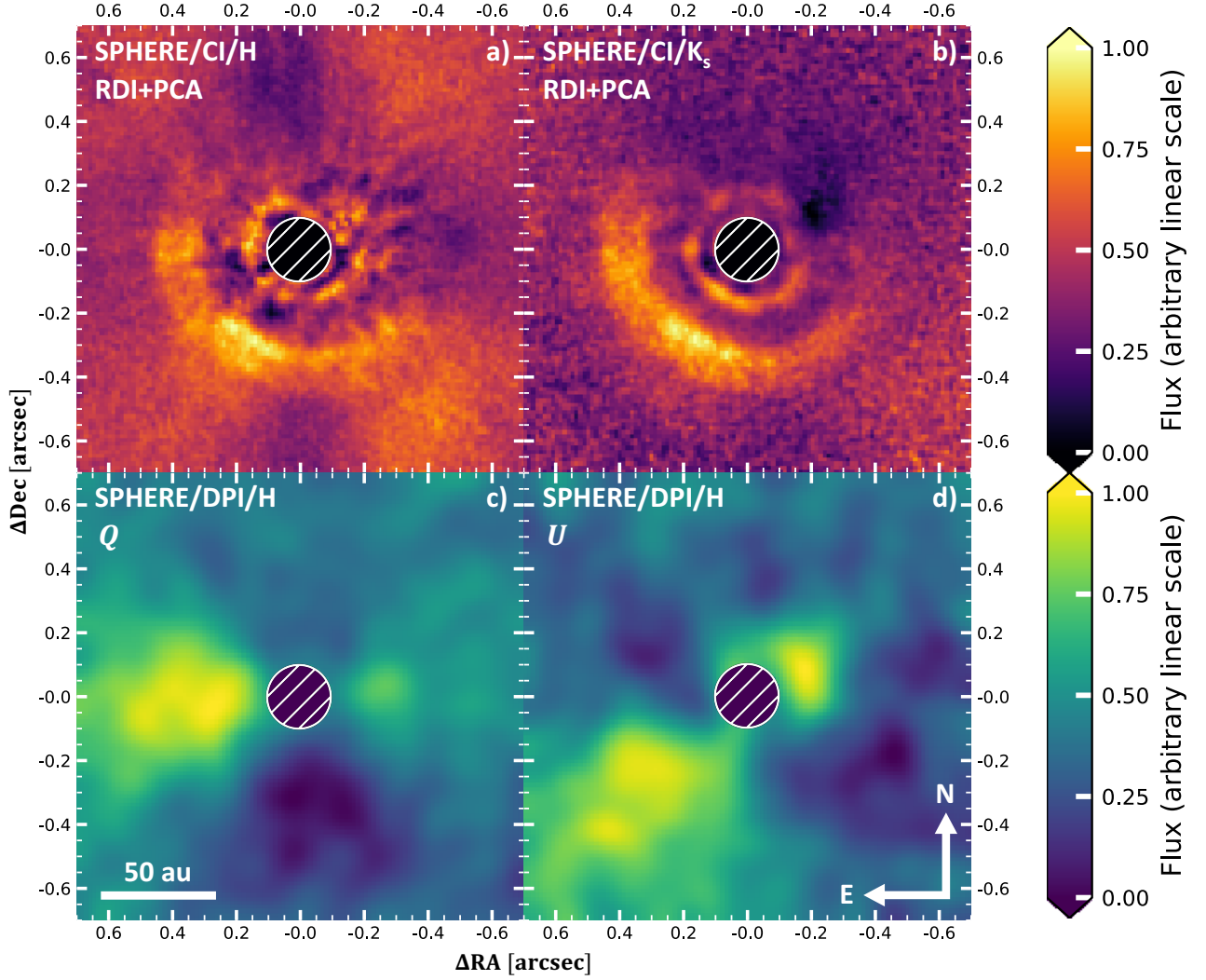


Fig. 1. Reduced SPHERE images of Wray 15-788. All frames show the same region on sky with a field of view of approximately $1''.39 \times 1''.39$. The star is positioned in the center of each image. An artificial mask with a diameter of ~ 196 mas is applied to obscure the coronagraph and leaking flux close to it. The images are scaled with r^2 according to the deprojected separation of the disk to star in the center of the image. The scaling is corrected for an inclination of 21° and a position angle of 76° as derived in Sect. 5.3.1. In each image north is up and east is left. An arbitrary linear color scale is applied, which is normalized to the maximum flux in each frame. Images **a** and **b** show the results obtained with SPHERE in classical imaging (CI) mode applying a broad H - and K_s -band filter, respectively. The stellar point spread function was reconstructed by a fit of 20 principal components obtained from a library of reference stars. In the bottom panel we present the results obtained from SPHERE dual-polarization imaging (DPI) data in H -band. Images **c** and **d** show the Stokes Q and U parameters for linear polarization, respectively. Both polarimetric results are smoothed with a Gaussian kernel having a full width at half maximum (FWHM) of ~ 50 mas. This is equivalent to the theoretical SPHERE FWHM in H -band.

ity

$$f = \frac{L_{\text{IR}}}{L_*}, \quad (1)$$

where L_{IR} and L_* denote the bolometric luminosities of the infrared excess and the star, respectively. To get accurate estimates of both bolometric luminosities, we fit the stellar spectrum and the infrared contribution to the SED due to circumstellar material individually with a suitable model.

Analyzing the SED with VOSA (Bayo et al. 2008) indicates an infrared excess for wavelengths longer than $W1$ ($\lambda_c^{W1} = 3.35 \mu\text{m}$). Thus, we only use the datapoints at wavelengths shorter than this to fit the spectrum of the star. For that purpose, we apply a Coelho stellar model (Coelho 2014) that depends on effective temperature, T_{eff} , surface gravity, $\log(g)$, as well as the metallicity parameters $[\text{Fe}/\text{H}]$ and $[\alpha/\text{Fe}]$ of the star. Furthermore, we assume a total extinction A_V in the range of

$0.5 \text{ mag} < A_V < 1.5 \text{ mag}$, in agreement with $A_V = 0.88 \pm 0.18 \text{ mag}$ as determined by Pecaut & Mamajek (2016) for Wray 15-788. The χ^2 fit yields a template stellar spectrum with $T_{\text{eff}} = 4250 \text{ K}$, $\log(g) = 4.5$, $[\text{Fe}/\text{H}] = 0$, $[\alpha/\text{Fe}] = 0$, and $A_V = 0.74$ which is represented by the blue line in Fig. 4. These model parameters agree very well with the stellar properties of Wray 15-788 determined by Pecaut & Mamajek (2016) and within the scope of this work as presented in Sect. 5.1. The red points in Fig. 4 show the fitted photometric datapoints from *APASS*, *Gaia*, *2MASS*, and *DENIS*, for which a de-reddening according to the best fit stellar model was applied. The gray squares and brown triangles represent the infrared flux of the system and upper limits to it, respectively.

To determine L_{IR} we focus on the excess at wavelengths longer than $2 \mu\text{m}$. First, we correct the available datapoints for the contamination by stellar flux using the best fit Coelho stellar model that we have found for the star. The corrected data is presented by the green dots in Fig. 4. To model the infrared SED

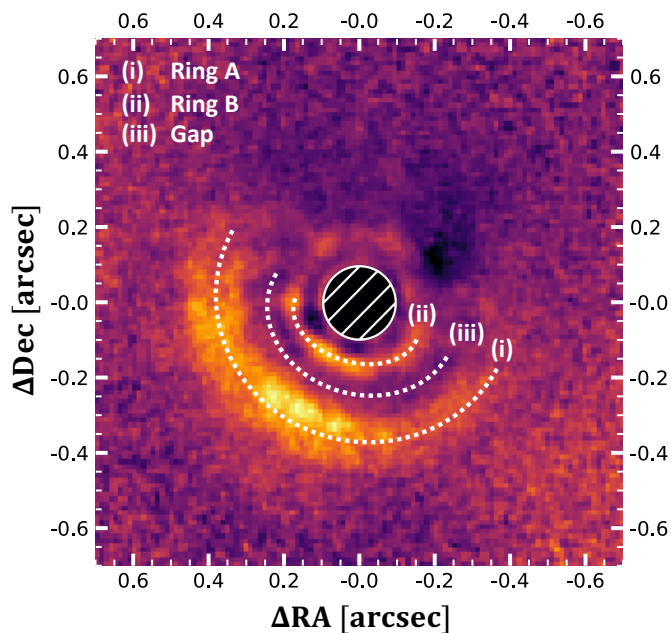


Fig. 2. Annotated version of Fig. 1 b. The discussed features of the disk are highlighted.

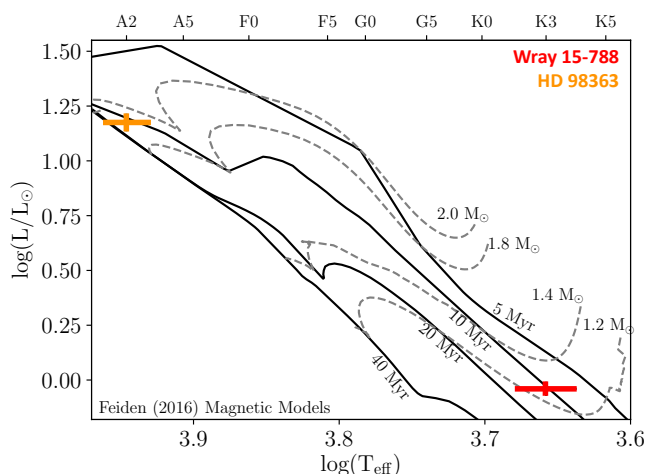


Fig. 3. Hertzsprung-Russell diagram for the binary system of Wray 15-788 and HD 98363. We plot pre-main sequence tracks and isochrones according to Feiden (2016) to constrain masses and ages of the companions.

of circumstellar material around Wray 15-788 we use three individual blackbodies: one to account for a hot, inner component at wavelengths between $2\mu\text{m}$ and $10\mu\text{m}$ and two additional blackbodies to characterize the colder, outer parts of the disk. The corrected data is fitted by the sum of these blackbody functions using a Levenberg–Marquardt non-linear least squares solver (Levenberg 1944; Marquardt 1963) and taking the inverse of each datapoint’s uncertainty as corresponding numerical weight. This yields a best fit result with effective blackbody temperatures of 969 K, 83 K, and 25 K, respectively. The individual blackbodies are indicated by the gray, dashed lines in Fig. 4 and their sum is represented by the solid, orange curve.

Integrating the stellar model and the fit of the infrared excess over the entire spectral range yields a fractional infrared luminosity of $f \approx 0.27$. Due to the incomplete SED for wavelengths

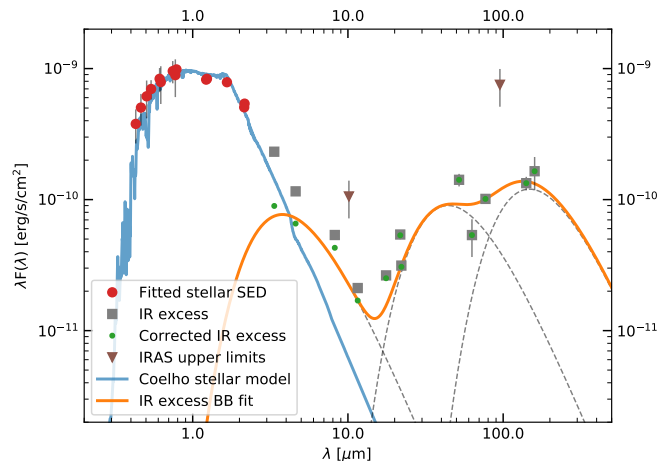


Fig. 4. De-reddened spectral energy distribution of Wray 15-788. The blue curve shows a Coelho stellar model (Coelho 2014) with $T_{\text{eff}} = 4250$ K, $\log(g) = 4.5$, $[\text{Fe}/\text{H}] = 0$, $[\alpha/\text{Fe}] = 0$, and $A_V = 0.74$ that is fitted to the red datapoints from *APASS*, *Gaia*, *2MASS*, and *DENIS* photometry. The gray squares denote flux measurements from *WISE*, *IRAS*, *AKARI/FIS*, as well as *AKARI/IRC* and the brown triangles provide upper limits from *IRAS*. Three blackbodies with $T_{\text{dust},1} = 969$ K, $T_{\text{dust},2} = 83$ K, and $T_{\text{dust},3} = 25$ K are simultaneously fitted to the green datapoints that denote the object’s far infrared excess, corrected for stellar contamination. The individual blackbody functions are indicated by the dashed, gray lines, whereas their sum is presented by the solid, orange curve.

longer than $160\mu\text{m}$ this value has to be interpreted as a lower threshold.

5.3. Imaging data

Both classical and dual-polarimetric imaging results confirm a resolved, asymmetrical, disk-like structure around Wray 15-788. Consequently, we try to quantify the reliability of the features detected in Fig. 1.

5.3.1. Ring A

Ring A of the disk is detected with SPHERE/CI in both *H*- and *K_s*-band and the butterfly patterns in Stokes *Q* and *U* frames from SPHERE/DPI are a strong confirmation of a scattering, disk-like structure around Wray 15-788. Due to the higher signal-to-noise ratio of the disk detection, we restrict our subsequent analyses to the *K_s*-band data.

Disk fitting

To determine the inclination of the disk, we fit *ring A* by an elliptical aperture. For that purpose, we use the SPHERE/CI *K_s*-band result as presented in Fig. 1 b.

We smooth the images with a Gaussian kernel having a FWHM of 55 mas, which corresponds to the theoretical size of the instrument’s PSF in *K_s*-band. To focus the fit only on present signal of the disk, an inner and outer mask are placed around *ring A*. The mask’s inner and outer radii are set to $0''.31$ and $0''.47$, respectively. Afterwards, we split the image in 100 azimuthal slices, centered at the star’s position. Within each slice, we determine the pixel of maximum flux. For rejection of background signal, we set a lower threshold that corresponds to the median

Table 3. Ellipse parameters.

| Parameter | Explanation |
|------------------------|---------------------------------------|
| $(\delta x, \delta y)$ | Center offset from the star position |
| a | Semi-major axis |
| b | Semi-minor axis |
| φ | Position angle of the semi-major axis |

Table 4. Best fit parameters of the ellipse.

| Parameter | Best fit value |
|-------------------------------|------------------|
| δx [pix] ^a | 0.96 ± 1.17 |
| δy [pix] | 1.12 ± 2.01 |
| a [pix] | 32.56 ± 0.81 |
| b [pix] | 30.39 ± 2.12 |
| φ [°] | 76 ± 16 |
| i [°] | 21 ± 6 |

Notes. ^(a) To convert pixels to projected separations in mas, the results must be multiplied with the pixel scale of the detector, which is 12.265 ± 0.009 mas per pixel in K_s -band.

flux at the pixel's separation to the star. Finally, an ellipse is fitted to the remaining pixels of maximum flux by a linear least squares algorithm according to the implementation of Fitzgibbon et al. (1999). We used a model of an arbitrary, two-dimensional ellipse with five free parameters δx , δy , a , b , φ . The meaning of these parameters is explained in Table 3. The disk inclination i can consequently be calculated as

$$i = \arccos\left(\frac{b}{a}\right). \quad (2)$$

To assess an estimate of the uncertainties on our best fit parameters we assume that the locations of the initial positions used for the fit are uncertain to the FWHM that was applied for smoothing. Therefore, we randomly sample the initial positions around the previously used values within a box with the size of the FWHM. We use a flat prior in both x and y direction and repeat the fitting procedure 10^6 times. We obtain symmetric posterior distributions of the ellipse parameters and use the standard deviation as an estimate for the statistical uncertainties of the fit parameters.

The best fit values and corresponding uncertainties of the ellipse parameters are presented in Table 4. The fitting yields a disk inclination of $i = 21^\circ \pm 6^\circ$ and a position angle of $\varphi = 76^\circ \pm 16^\circ$. These constraints rather loose due to the low inclination of the system and because the datapoints used for the fit sample less than half of an ellipse. Additional high-quality data is required to confine this parameter space.

Disk signal-to-noise ratio estimation

As presented in Fig. 1, the azimuthal brightness profile of *ring A* varies strongly. Starting north of the star, the disk flux increases with increasing position angle ϕ . The maximum intensity of this ring is located southeast of the star. Thereafter, the flux decreases with increasing position angle until the disk signal cannot be distinguished from the background noise.

We aim to determine a range of position angles, in which we have a significant detection of scattered light flux from *ring*

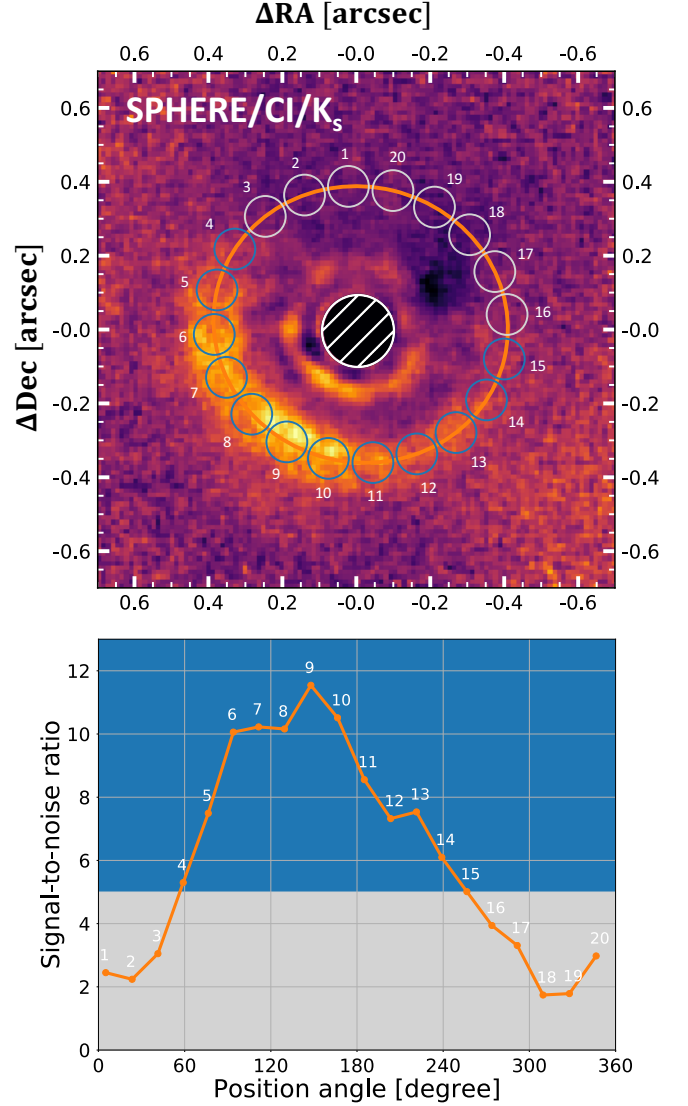


Fig. 5. *Top:* Signal-to-noise ratio measurements in circular apertures around the best fit ellipse (orange line) for the K_s -band data from Sect. 5.3.1. The blue apertures contain flux of *ring A* according to the applied 5σ criterion, whereas the gray apertures reside within the background dominated regime. *Bottom:* Signal-to-noise ratio within the circular apertures from the top panel. We sort the apertures by position angle. The gray and blue areas mark the regimes below and above the 5σ threshold for distinction of background and disk apertures, respectively.

A. Therefore, we use the best fit ellipse that we have derived before and distribute evenly spaced circular apertures along it as indicated in Fig. 5. We measure the mean flux and standard deviation inside each individual circular aperture. The average flux values μ_i provide us an estimate of the signal at the position angle of the corresponding aperture. To get an estimate of the background noise, we perform a sigma clipping on the array of aperture fluxes. For the clipping we run five iterations with no lower threshold and an upper threshold of 1σ to exclude strong contamination by disk flux. After this selection, we calculate the average of the remaining standard deviations for estimating the background noise σ_{bg} . The SNR of each individual aperture is calculated as

$$SNR_i = \frac{\mu_i}{\sigma_{bg}}. \quad (3)$$

We apply an arbitrary threshold of $\text{SNR}_i > 5$ for selection of disk apertures and rejection of background signal. This selection criterion, however, agrees very well with the range of position angles, where disk signal can still be distinguished from background noise by visual inspection (see Fig. 1 b).

The bottom panel of Fig. 5 shows the measured SNR inside each aperture and compares these to the applied threshold criterion. Datapoints in the blue regime of the plot refer to apertures above the threshold and are, therefore, considered to indicate a detection of scattered light flux from *ring A*. The gray regime, however, represents apertures that are dominated by background noise. This color scheme coincides with the colors chosen for the circular apertures in the top panel of the figure. Considering these blue apertures, we derive a range of $60^\circ \lesssim \phi \lesssim 240^\circ$, in which we are confident at 5σ level to detect scattered light flux of the disk.

Furthermore, we create an inclination-corrected polar projection of the SPHERE/CI results in K_s -band as presented in the left panel of Fig. 6. Averaging over the position angles within the derived range of $60^\circ \lesssim \phi \lesssim 240^\circ$ (indicated by the white, dashed lines) yields the radial brightness profile presented by the blue curve in the right panel of Fig. 6. The gray curve presents the average over the remaining range of position angles, in which we do not detect significant disk signal. From these profiles, it becomes clear that we resolve both the gap and *ring A*. The latter even shows some hints for substructures, as the averaged flux does not decrease as steeply in radially outward direction as it does towards the inward gap. Even beyond deprojected separations of $0''.5$ the average flux of the disk signal is significantly larger than the average background noise. This is a strong confirmation for scattering material beyond the sharp edge of *ring A*, which was already implied by the DPI data presented in Fig. 1 c and d.

Additionally, the polar deprojection allows us to estimate physical separations of the disk features that we have detected: *Ring A* has its peak of scattered light intensity at ~ 56 au, the scattered light flux is lowest inside the gap at ~ 35 au, and *ring B* has a separation of ~ 28 au.

5.3.2. Ring B

To quantify the significance of the detected inner substructure from the SPHERE imagery, we investigate the polar projection presented in the left panel of Fig. 6. In between the two white, dashed lines at a deprojected separation of $\sim 0''.2$, *ring B* appears to be partly parallel to the resolved *ring A* and even has a similar azimuthal brightness distribution. Therefore, it is possible that we detect parts of an inner substructure with similar scattering properties. In the remaining range of position angles, however, the flux received from *ring B* is significantly smaller and its deprojected radial separation varies strongly. This is an indication for a symmetrical, probably non-astrophysical residual around the coronagraph that gets distorted by the inclination correction that we perform to create Fig. 6.

To test this hypothesis, we compare our result to data from our reference library, obtained with the same observational setup. These data are reduced analogously to the approach we describe in Sect. 3. For each target we apply RDI in combination with PCA and we fit 20 components for modeling the stellar PSF. All residuals are averaged individually for both filters and to enhance the comparability to our previous results from Fig. 1, we apply the same radial scaling and masking of the innermost region. However, we do not perform any de-rotation of the images. Because all data was obtained in pupil stabilized mode, this

approach ensures proper alignment of potential instrumental artifacts. These reference images in H - and K_s -band are presented in Fig. 7.

In both reference images we detect some features close to the coronagraph. Whereas the H -band data shows a rather unstructured speckle pattern similar to the science result in that filter (compare to Fig. 1 a), the K_s -band reference residuals reveal a faint inner ring at the same projected radial separation of ~ 170 mas. But *ring B* that we detect around Wray 15-788 is significantly brighter in the southeast than the residuals from the reference library. Northwest of the star, however, the intensity of *ring B* is equal for Wray 15-788 and the reference stars. This is consolidating our claim that we actually detect scattered light flux of an inner substructure southwest of the star. To quantify this observation, we perform photometry in circular apertures distributed alongside *ring B* as indicated in the top panel of Fig. 8. We choose a radial separation of ~ 170 mas to the star and each aperture has a radius of ~ 25 mas, which corresponds to the measured width of *ring B*. These measurements are performed for both filter combinations and the corresponding reference results. We determine the average flux and standard deviation per aperture and plot these as a function of position angle as presented in the bottom panel of Fig. 8. Whereas in H -band no strong differences between the flux around Wray 15-788 and the reference image can be detected, we observe a significant peak in K_s -band. Within a range of position angles of $120^\circ \lesssim \phi \lesssim 240^\circ$ the flux measured in the apertures on *ring B* around Wray 15-788 is greater compared to the flux from the reference image within the same range of position angles. The determined angular interval lies within the one, where we detect *ring A* with a SNR greater than 5σ . This strengthens the claim that we actually detect parts of an inner substructure around Wray 15-788. Because we do not spatially resolve these structures, we cannot make an accurate estimate of its inclination.

Even though Fig. 6 implies the detection of another gap interior to *ring B*, we do not trust this feature, because it is placed very close to the inner working angle (IWA) of the coronagraph of 100 mas (Wilby et al. in prep.). For this reason we consider it to be an artifact caused by our post-processing strategy.

5.3.3. Gap

For the CI results we detect a significant decrease of flux interior to *ring A*. Depending on the position angle, this radial gradient is steepest at a projected separation of ~ 250 mas. We do not recover this drop in scattered light surface brightness from the polarimetric dataset, but there are several reasons to explain this behavior (e.g., the non-optimal weather conditions or the smoothing with a Gaussian kernel). Furthermore, we can conclude from the polar deprojection of the disk in Fig. 6 that we are able to spatially resolve this radial drop in intensity. Because we detect this decrease of scattered light flux even in data processed without proper subtraction of the stellar PSF by RDI+PCA (see Appendix B.1), we conclude that it is a real phenomenon. Possible explanations for this very certain dip in surface brightness are either a shadowed region or a physical cavity within the disk.

5.3.4. Detection limits

To derive mass limits of an undetected companion to Wray 15-788, we calculate 5σ contrast curves using the standard routine of the PynPoint package (Stolker et al. 2019). Artificial companions are obtained from the non-coronagraphic flux images

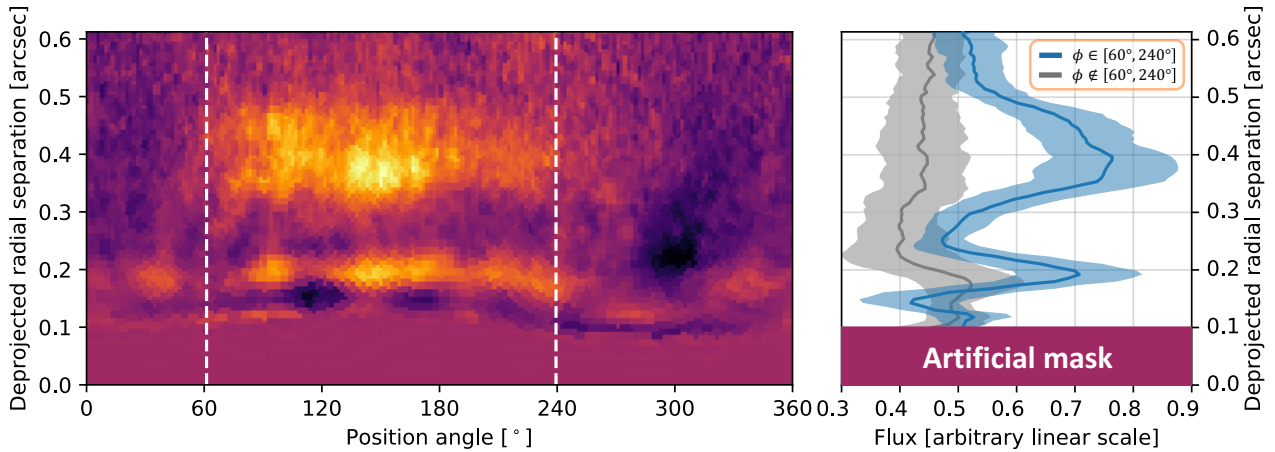


Fig. 6. *Left panel:* Polar projection of the SPHERE/CI result in K_s -band. The image is corrected for the offset and the inclination of the best fit ellipse to *ring A*. The white, dashed lines indicate the range of position angles, in which we detect scattered light flux from *ring A* with a signal-to-noise ratio larger than 5. *Right panel:* Radial brightness profile of the disk and background noise. The blue curve shows the averaged disk signal for position angles in the range of $60^\circ \leq \phi \leq 240^\circ$ and the gray curve represents the average noise over all remaining position angles. The envelopes indicate the corresponding standard deviations.

that we have taken alongside our science observations. These are scaled to correct for the difference in exposure times and the attenuation of a neutral density filter. The injection is performed for six evenly spaced azimuthal directions and radial separations ranging from $0''.15$ to $1''$ with a step size of 20 mas. We present the 5σ detection limits for both CI filters in Fig. 9. Close to the star, we apply a correction to account for small sample statistics according to Mawet et al. (2014). The conversion from magnitude contrast to a detectable mass threshold is performed using AMES-Cond³ atmospheric models of 11 Myr old substellar objects (Allard et al. 2001; Baraffe et al. 2003). We indicate the position of the two rings and the gap in blue and gray, respectively. Because the structures are not detected face-on, there are small spatial overlaps between rings and the gap. At the gap's center we are sensitive to companions as massive as $10 M_{\text{jup}}$ and $15 M_{\text{jup}}$ in H - and K_s -band, respectively. At separations larger than $1''$, we can rule out companions more massive than $4 M_{\text{jup}}$. We did not apply any correction for reddening and extinction by interstellar matter or disk material in our analysis.

6. Discussion

6.1. SED analysis

Pecaut & Mamajek (2016) rank Wray 15-788 as a potential host of a protoplanetary disk based on two criteria: (i) the $H\alpha$ emission as an indicator of accretion from a gas-rich disk and (ii) the presence of an infrared excess in its SED indicative of dust grains. The $\text{EW}(H\alpha)$ threshold for accretion from Barrado y Navascués & Martín (2003) for a K3 star is 4.1 \AA ; the measured $\text{EW}(H\alpha)$ from Pecaut & Mamajek (2016) is 10.3 \AA . The full width at 10% max of the line is 430 km/s (Pecaut, private communication 2018), which exceeds the empirical criterion for accretion of 270 km/s (White & Basri 2003) and, thus, is consistent with ongoing accretion. Furthermore, Pecaut & Mamajek (2016) derive the extent of the infrared excess by determining K_s-W3 and K_s-W4 colors from 2MASS (Henden et al. 2012) and WISE (Cutri et al. 2012b) magnitudes (see Table 1). According to the

³ The latest version of these models were obtained from <https://www.phoenix.ens-lyon.fr/Grids/AMES-Cond>

empirical threshold determined by Luhman & Mamajek (2012), a protoplanetary disk is expected to have excesses exceeding $K_s-W3 > 1.5$ and $K_s-W4 > 3.2$. With $K_s-W3 = 1.76 \pm 0.04$ and $K_s-W4 = 4.3 \pm 0.04$, Wray 15-788 clearly meets these criteria.

The conclusion that Wray 15-788 hosts a protoplanetary disk is clearly supported by the analysis of the object's SED as presented in Sect 5.2. Comparison of the derived fractional infrared luminosity $f \gtrsim 0.27$ with empirical thresholds of Dominik et al. (2003) and Lagrange et al. (2000), strongly imposes that Wray 15-788 harbors a gas-rich protoplanetary disk rather than a debris disk where most of the gas has already dissipated. Indeed, usual fractional infrared luminosities of the latter category are in all known cases definitely smaller than 10^{-2} . So, Wray 15-788 exceeds this threshold by more than one order of magnitude.

Furthermore, the fit of the flux at wavelengths longer than $2 \mu\text{m}$ as presented in Fig. 4 clearly illustrates that the infrared SED of the system cannot be described by a single belt model alone. The excess at near infrared wavelengths ($2 \mu\text{m} < \lambda < 10 \mu\text{m}$), modeled by a blackbody with an effective temperature of 969 K, strongly indicates the presence of a hot, inner component of the disk around the star (e.g. Tilling et al. 2012). Due to the high effective temperature this inner component must be located close to the dust sublimation radius and, therefore, definitely interior to the IWA of the applied coronagraph. Thus, we can rule out at high confidence that *ring B*, as potentiality detected in the imaging data, is equivalent to this hot inner component of the disk. Comparing the SPHERE imagery with the object's SED suggests that *ring A* and *B* are represented by the infrared excess at wavelengths longer than $10 \mu\text{m}$.

Around $10 \mu\text{m}$ a dip in the SED is apparent that is followed by a positive gradient towards longer wavelengths. These characteristics of the SED impose a physical, dust depleted cavity inside the disk that is enclosed by an extended, colder component of disk material. For these reasons, we conclude that Wray 15-788 hosts a protoplanetary disk at a transition stage (Strom et al. 1989; Furlan et al. 2009).

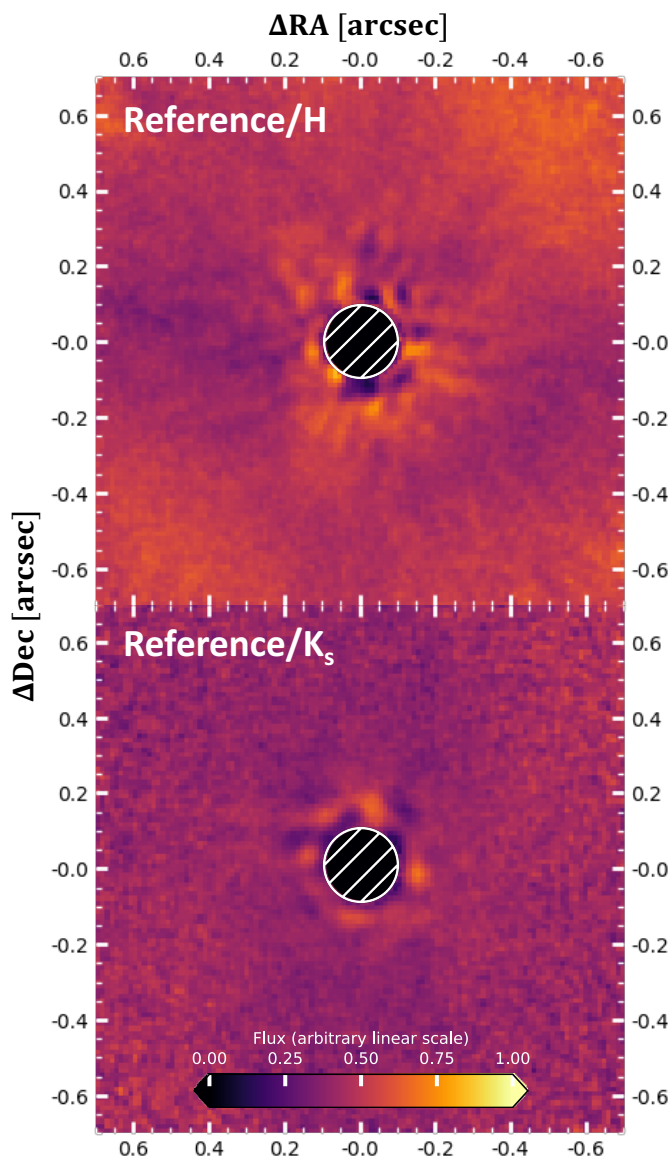


Fig. 7. Comparison to average images obtained from reduced reference library targets in both H - (top) and K_s -band (bottom).

6.2. Disk morphology

The disk around Wray15-788 appears highly asymmetric with flux only detected on the southeastern side. Because we can detect this asymmetry in the DPI data as well and even in the CI data processed without proper subtraction of the stellar PSF, we can rule out that this appearance is an artifact of our post-processing. These alternative reductions are presented in Appendix B. Due to the low inclination of the disk our observation probes only a limited range of scattering angles, which should not be significantly smaller than $\sim 50^\circ$. In this range of scattering angles the scattering phase functions of typical disks are flat (see Hughes et al. 2018, for an extensive overview). Thus we should receive scattered light from all azimuthal positions of the disk. This is indeed true even for slightly more inclined debris and gas-rich disks, such as HD 181327 ($i \approx 32^\circ$, e.g., Soummer et al. 2012), PDS 66 ($i \approx 32^\circ$, e.g., Schneider et al. 2014; Wolff et al. 2016), V4046 Sgr ($i \approx 34^\circ$, e.g., Rapson et al. 2015), or HD 100453 ($i \approx 38^\circ$, e.g., Benisty et al. 2017). For PDS 66, Wolff et al. (2016) measure contrasts in scattered light brightness of 2.1

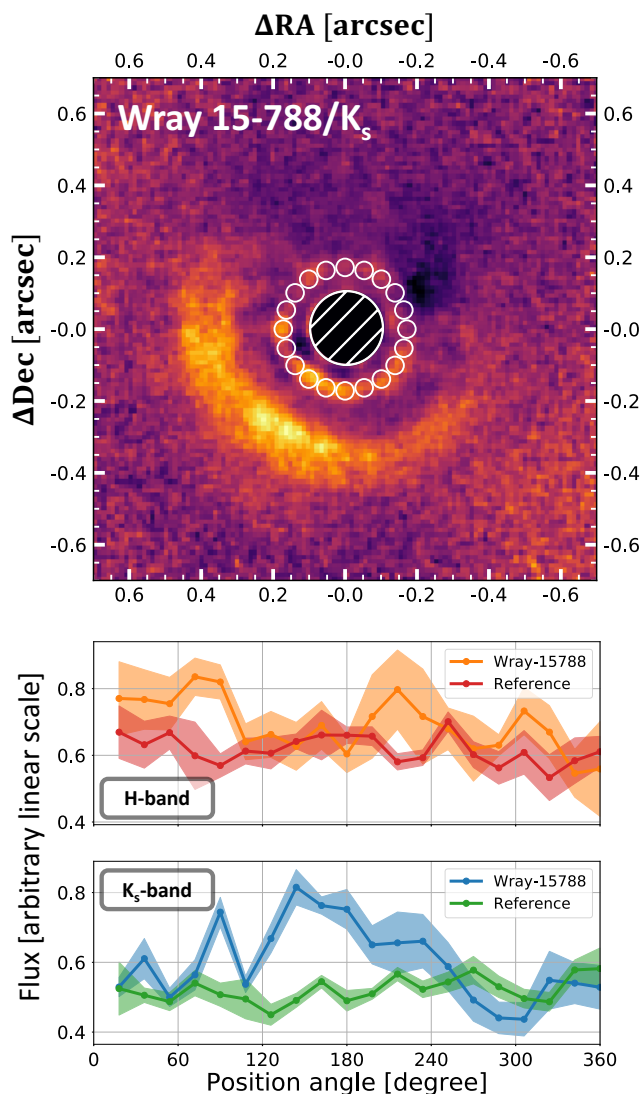


Fig. 8. Comparison to average images obtained from reduced reference library targets. *Top:* The white circles indicate the locations of the flux apertures that are distributed alongside *ring B*. *Bottom:* Flux measurements in the apertures from the top panel as a function of position angle. The solid lines correspond to the average flux per aperture. The envelope indicates the corresponding standard deviation.

and 1.6 for H - and K_1 -band, respectively, between near and far sides of the disk. Adopting this contrast ratio for Wray 15-788 shows that we should detect the far side of the disk (northwestern part) at a SNR greater than 5, because the near side (southeastern part) is detected at a SNR of approximately 12. As presented in Fig. 5 this is obviously not the case. Although we cannot fully rule out the possibility that the asymmetry is caused by a larger contrast ratio between near and far side of the disk so that the SNR in the northwest drops below our detection ability, it seems unlikely that the apparent morphology is caused by scattering phase function effects.

We thus can conclude that the asymmetry is either caused by a strong azimuthal variation in surface density or scale height of the disk, or that a shadow is cast on *ring A* by unresolved disk structures, interior to the structures we detect in our SPHERE observations. Azimuthal variations in surface density are regularly observed at longer (millimeter) wavelengths with ALMA, e.g. around HD 142527 (Pérez et al. 2014) or V1247 Ori (Kraus et al.

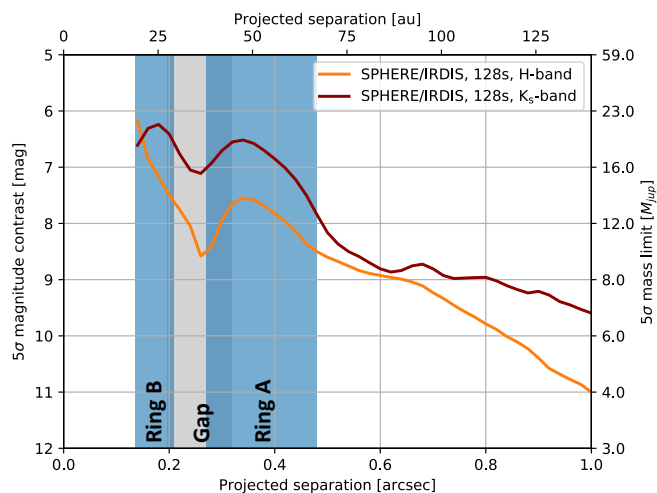


Fig. 9. Magnitude and mass limits (5σ) up to $1''$ around Wray 15-788. The positions of the two rings and the gap are indicated in blue and gray, respectively. The magnitude contrast is converted to an upper mass limit by AMES-Cond models for 11 Myr old objects. Inside the gap we are sensitive to companions as massive as $10 M_{\text{jup}}$ (H -band) and $15 M_{\text{jup}}$ (K_s -band).

2017). These azimuthal asymmetries are hypothesized to originate from pressure bumps in the gas that trap large, millimeter-sized dust particles in the disk midplane. With SPHERE/IRDIS, however, we trace small, micron-sized dust particles at the disk surface which are much less affected by particle trapping in the disk (see for example Pinilla et al. 2016). It is thus unlikely that we would observe an extreme asymmetry in scattered light. This effect can indeed be observed, e.g. for the HD 142527 transition disk where the strong azimuthal asymmetry in large dust grains is not visible in scattered light (Avenhaus et al. 2014, Casassus et al. 2015).

This leaves us with the hypothesis that the northwestern side of the visible disk structure is possibly shadowed by an unresolved part of the disk at separations not probed by the SPHERE observations. This can be the case if the inner part of the disk is misaligned with respect to the visible structures. For example, according to Price et al. (2018), a (sub-)stellar companion may cause this misalignment of an inner disk. Such a misalignment can produce a variety of features from sharp, dark lanes, as observed in the disks around HD 142527 (Avenhaus et al. 2014), HD 100453 (Benisty et al. 2017), or HD 135344B (Stolker et al. 2016), to broader wedges as reported for PDS 66 (Wolff et al. 2016) or TW Hya (Debes et al. 2017). Recently, Benisty et al. (2018) showed scattered light images of the circumstellar disk around HD 143006, in which analogously to the current case, approximately half of the outer ring is shadowed by inner disk structures and is thus not detected in scattered light. As presented in Sect. 5.2, the analysis of the object’s SED strongly indicates the presence of a hot, inner component of the disk, just as required for the proposed shadowing scenario. However, the absence of narrow lanes implies that if present, the shadowing must be due to a very small misalignment. To confirm this hypothesis, however, deeper data is required (e.g. a time series that could show the rotation of the shadowed regions around the star).

6.3. Comparison with HD 98363

As studied by Chen et al. (2012) and Moór et al. (2017), the primary star HD 98363 hosts a gas-poor debris disk. The detected disk around Wray 15-788, however, does not appear to be at this stage of evolution. Due to the lack of dust, debris disks are usually optically thin (Wyatt et al. 2015), what makes them hard to detect in near infrared scattered light. However, we have a detection in only two minutes of integration, which is at least unusual, if Wray 15-788 was also hosting a gas-poor, debris disk. This agrees with the conclusion of Pecaut & Mamajek (2016), who ranked the star as a potential host of a protoplanetary disk based on its $H\alpha$ emission and infrared excess from *WISE* photometry.

This brings up interesting questions about the evolution of the systems. Assuming both have formed at approximately the same time with similar initial conditions, it is peculiar that the disk around HD 98363 is already more evolved compared to the one around Wray 15-788. As studied by Ribas et al. (2015) there seems to be a trend of decreasing protoplanetary disk lifetimes with increasing mass of the star. In their empirical study, however, they only compare the evolutionary stages of disks around stars above and below $2 M_{\odot}$. Because both Wray 15-788 and HD 98363 fall into the latter category, their conclusions cannot directly be applied to our sample. Another explanation for the different nature of the disks around both stars might be the presence of multiple planetary companions around Wray 15-788. These can act as traps for dust particles leading to a radial segregation of different sized dust particles as studied by Pinilla et al. (2015). To further explore possible scenarios, additional data on Wray 15-788 is necessary. Especially, high-resolution (sub)-millimeter observations are essential to confirm the disk’s status as a gas-rich protoplanetary disk.

7. Conclusions

For the first time, we resolve a transition disk around young K3IV star Wray 15-788 in scattered light with both SPHERE/CI and SPHERE/DPI data. SED analysis suggests that the star hosts a hot, inner disk located interior to the IWA of the presented imaging data. An excess at wavelengths longer than $10 \mu\text{m}$ indicates additional disk material at larger separations from the star. In agreement with this far infrared SED, we identify an arc at a projected separation of ~ 370 mas and a potential inner ring at ~ 170 mas in the SPHERE data. These two features are separated by a resolved region of significantly reduced flux. From the outer arc, which is detected above 5σ within a range of position angles of $60^{\circ} \lesssim \phi \lesssim 240^{\circ}$, we determine a disk inclination of $i = 21^{\circ} \pm 6^{\circ}$ and a position angle of $\varphi = 76^{\circ} \pm 16^{\circ}$. Correction for this inclination places the outer ring, the gap, and the inner substructures from the imaging data at approximate physical separations of 56 au, 35 au, and 28 au, respectively.

Although we detect the disk at low inclination, large parts of the the outer ring remain hidden below the background noise. This peculiar appearance may be caused by a shadow that is cast from unresolved inner substructures which are misaligned with respect to the outer ring. This scenario is in very good agreement with the SED of Wray 15-788, which shows clear evidence for a inner disk with an effective temperature of 969 K. The misalignment of this inner disk may be caused by an undetected sub-stellar companion. From our 5σ detection thresholds we derive an upper mass limit of $10 M_{\text{jup}}$ for a companion inside the detected gap. At projected separations larger than $1''$ we can rule out companions more massive than $4 M_{\text{jup}}$. We can not, however,

rule out the possibility that half of the disk is faint in the north-west and that our SNR is not high enough to detect it.

Further, we found Wray 15-788 to be companion to the A2V star HD 98363. Therefore, Wray 15-788 is actually HD 98363 B at a separation of $\sim 50''$ (≈ 6900 au) to the primary. Even though both objects have the same age of 11^{+16}_{-7} Myr, the primary hosts a debris disk, where most of the primordial gas has already dissipated, whereas we are confident to detect a less evolved protoplanetary disk around Wray 15-788. Possible undetected companions may be responsible for trapping of the dust, leading to the different kind of disks within the binary system of HD 98363 and Wray 15-788.

Further, deeper observations need to be conducted to better understand the disk's peculiar morphology and to find possible planetary mass companions. To confirm the detection of an inner ring and to constrain the inclination of the disk, a deeper, polarimetric observation is necessary. Additional constraints to the disk's composition, the presence of gas, and the sizes of its dust grains can be set with sub-millimeter observations making use of the Atacama Large Millimeter/submillimeter Array (ALMA).

Acknowledgements. The research of A. J. Bohn and F. Snik leading to these results has received funding from the European Research Council under ERC Starting Grant agreement 678194 (FALCONER). M.B. acknowledges funding from ANR of France under contract number ANR-16-CE31-0013 (Planet Forming disks). Part of this research was carried out at the Jet Propulsion Laboratory, California Institute of Technology, under a contract with the National Aeronautics and Space Administration. This publication makes use of VOSA, developed under the Spanish Virtual Observatory project supported from the Spanish MINECO through grant AyA2017-84089. This research has made use of the SIMBAD database, operated at CDS, Strasbourg, France (Wenger et al. 2000). To achieve the scientific results presented in this article we made use of the *Python* programming language⁴, especially the *SciPy* (Jones et al. 2001–), *NumPy* (Oliphant 2006), *Matplotlib* (Hunter 2007), *scikit-image* (Van der Walt et al. 2014), *scikit-learn* (Pedregosa et al. 2012), *photutils* (Bradley et al. 2016), and *astropy* (Astropy Collaboration et al. 2013, 2018) packages.

References

- Allard, F., Hauschildt, P. H., Alexander, D. R., Tamanai, A., & Schweitzer, A. 2001, *ApJ*, 556, 357
- Amara, A. & Quanz, S. P. 2012, *MNRAS*, 427, 948
- Andrews, S. M., Wilner, D. J., Hughes, A. M., et al. 2012, *ApJ*, 744, 162
- Astropy Collaboration, Price-Whelan, A. M., Sipőcz, B. M., et al. 2018, *AJ*, 156, 123
- Astropy Collaboration, Robitaille, T. P., Tollerud, E. J., et al. 2013, *A&A*, 558, A33
- Avenhaus, H., Quanz, S. P., Garufi, A., et al. 2018, *ArXiv e-prints*, arXiv:1803.10882
- Avenhaus, H., Quanz, S. P., Schmid, H. M., et al. 2014, *ApJ*, 781, 87
- Bailer-Jones, C. A. L., Rybizki, J., Founesneau, M., Mantelet, G., & Andrae, R. 2018, *AJ*, 156, 58
- Baraffe, I., Chabrier, G., Barman, T. S., Allard, F., & Hauschildt, P. H. 2003, *A&A*, 402, 701
- Barrado y Navascués, D. & Martín, E. L. 2003, *AJ*, 126, 2997
- Bayo, A., Rodrigo, C., Barrado Y Navascués, D., et al. 2008, *A&A*, 492, 277
- Benisty, M., Juhasz, A., Facchini, S., et al. 2018, *ArXiv e-prints*, arXiv:1809.01082
- Benisty, M., Stolker, T., Pohl, A., et al. 2017, *A&A*, 597, A42
- Beuzit, J.-L., Feldt, M., Dohlen, K., et al. 2008, in *Ground-based and Airborne Instrumentation for Astronomy II*, Vol. 7014, 701418
- Bradley, L., Sipocz, B., Robitaille, T., et al. 2016, *Photutils: Photometry tools*
- Carbillet, M., Bendjoya, P., Abe, L., et al. 2011, *Experimental Astronomy*, 30, 39
- Casassus, S., Wright, C. M., Marino, S., et al. 2015, *ApJ*, 812, 126
- Chen, C. H., Pecauc, M., Mamajek, E. E., Su, K. Y. L., & Bitner, M. 2012, *ApJ*, 756, 133
- Choquet, E., Hagan, J. B., Pueyo, L., et al. 2014, in *Exploring the Formation and Evolution of Planetary Systems*, Vol. 299, 30–31
- Coelho, P. R. T. 2014, *MNRAS*, 440, 1027
- Cutri, R. M., Skrutskie, M. F., van Dyk, S., et al. 2012a, *VizieR Online Data Catalog*, II/281
- Cutri, R. M. et al. 2012b, *VizieR Online Data Catalog*, II/311
- de Zeeuw, P. T., Hoogerwerf, R., de Bruijne, J. H. J., Brown, A. G. A., & Blaauw, A. 1999, *AJ*, 117, 354
- Debes, J. H., Poteet, C. A., Jang-Condell, H., et al. 2017, *ApJ*, 835, 205
- Dohlen, K., Langlois, M., Saisse, M., et al. 2008, in *Proc. SPIE*, Vol. 7014, *Ground-based and Airborne Instrumentation for Astronomy II*, 70143L
- Dominik, C., Dullemond, C. P., Waters, L. B. F. M., & Walch, S. 2003, *A&A*, 398, 607
- Epchtein, N., de Batz, B., Capolani, L., et al. 1997, *The Messenger*, 87, 27
- Feiden, G. A. 2016, *A&A*, 593, A99
- Fitzgibbon, A., Pilu, M., & Fisher, R. B. 1999, *IEEE Trans. Pattern Anal. Mach. Intell.*, 21, 476
- Furlan, E., Watson, D. M., McClure, M. K., et al. 2009, *ApJ*, 703, 1964
- Fusco, T., Rousset, G., Sauvage, J.-F., et al. 2006, *Optics Express*, 14, 7515
- Gaia Collaboration, Brown, A. G. A., Vallenari, A., et al. 2018, *ArXiv e-prints*, arXiv:1804.09365
- Ginski, C., Stolker, T., Pinilla, P., et al. 2016, *A&A*, 595, A112
- Goldreich, P. & Ward, W. R. 1973, *ApJ*, 183, 1051
- Guerrí, G., Daban, J.-B., Robbe-Dubois, S., et al. 2011, *Experimental Astronomy*, 30, 59
- Henden, A. & Munari, U. 2014, *Contributions of the Astronomical Observatory Skalnaté Pleso*, 43, 518
- Henden, A. A., Levine, S. E., Terrell, D., Smith, T. C., & Welch, D. 2012, *Journal of the American Association of Variable Star Observers (JAAVSO)*, 40, 430
- Henize, K. G. 1976, *The Astrophysical Journal Supplement Series*, 30, 491
- Høg, E., Fabricius, C., Makarov, V. V., et al. 2000, *A&A*, 355, L27
- Houk, N. & Cowley, A. P. 1975, *University of Michigan Catalogue of two-dimensional spectral types for the HD stars. Volume I. Declinations -90 to -53 f0.*
- Hughes, A. M., Duchêne, G., & Matthews, B. C. 2018, *ARA&A*, 56, 541
- Hunter, J. D. 2007, *Computing in Science and Engineering*, 9, 90
- Ishihara, D., Onaka, T., Katata, H., et al. 2010, *A&A*, 514, A1
- Jones, E., Oliphant, T., Peterson, P., et al. 2001–, *SciPy: Open source scientific tools for Python*, [Online; accessed <today>]
- Kawada, M., Baba, H., Barthel, P. D., et al. 2007, *Publications of the Astronomical Society of Japan*, 59, S389
- Kraus, S., Kreplin, A., Fukugawa, M., et al. 2017, *ApJ*, 848, L11
- Lafrenière, D., Marois, C., Doyon, R., Nadeau, D., & Artigau, É. 2007, *ApJ*, 660, 770
- Lagrange, A.-M., Backman, D. E., & Artymowicz, P. 2000, *Protostars and Planets IV*, 639
- Langlois, M., Dohlen, K., Vigan, A., et al. 2014, in *Proc. SPIE*, Vol. 9147, *Ground-based and Airborne Instrumentation for Astronomy V*, 91471R
- Langlois, M., Vigan, A., Moutou, C., et al. 2013, in *Proceedings of the Third AO4ELT Conference*, 63
- Levenberg, K. 1944, *Quarterly of applied mathematics*, 2, 164
- Luhman, K. L. & Mamajek, E. E. 2012, *ApJ*, 758, 31
- Macintosh, B., Graham, J., Palmer, D., et al. 2006, in *Society of Photo-Optical Instrumentation Engineers (SPIE) Conference Series*, Vol. 6272, 62720L
- Maire, A.-L., Langlois, M., Dohlen, K., et al. 2016, in *Ground-based and Airborne Instrumentation for Astronomy VI*, Vol. 9908, 990834
- Mamajek, E. E., Pecauc, M. J., Nguyen, D. C., & Bubar, E. J. 2013, in *Protostars and Planets VI Posters*
- Marois, C., Lafrenière, D., Doyon, R., Macintosh, B., & Nadeau, D. 2006, *ApJ*, 641, 556
- Marquardt, D. W. 1963, *Journal of the society for Industrial and Applied Mathematics*, 11, 431
- Maschberger, T. 2013, *MNRAS*, 429, 1725
- Matsuyama, I., Johnstone, D., & Hartmann, L. 2003, *ApJ*, 582, 893
- Mawet, D., Milli, J., Wahhaj, Z., et al. 2014, *ApJ*, 792, 97
- Millar-Blanchaer, M. A., Esposito, T. M., Stahl, K., et al. 2017, in *Society of Photo-Optical Instrumentation Engineers (SPIE) Conference Series*, Vol. 10407, 104070V
- Moór, A., Curé, M., Kóspál, Á., et al. 2017, *ApJ*, 849, 123
- Murakami, H., Baba, H., Barthel, P., et al. 2007, *Publications of the Astronomical Society of Japan*, 59, S369
- Neugebauer, G., Habing, H. J., van Duinen, R., et al. 1984, *ApJ*, 278, L1
- Oliphant, T. E. 2006, *A guide to NumPy*, Vol. 1 (Trelgol Publishing USA)
- Pecauc, M. J. & Mamajek, E. E. 2016, *MNRAS*, 461, 794
- Pedregosa, F., Varoquaux, G., Gramfort, A., et al. 2012, *ArXiv e-prints*, arXiv:1201.0490
- Pérez, L. M., Isella, A., Carpenter, J. M., & Chandler, C. J. 2014, *ApJ*, 783, L13
- Petit, C., Sauvage, J.-F., Fusco, T., et al. 2014, in *Proc. SPIE*, Vol. 9148, *Adaptive Optics Systems IV*, 91480O
- Pinilla, P., de Juan Ovelar, M., Ataiee, S., et al. 2015, *A&A*, 573, A9
- Pinilla, P., Klarmann, L., Birnstiel, T., et al. 2016, *A&A*, 585, A35
- Price, D. J., Cuello, N., Pinte, C., et al. 2018, *MNRAS*, 477, 1270
- Rapson, V. A., Kastner, J. H., Andrews, S. M., et al. 2015, *ApJ*, 803, L10

⁴ Python Software Foundation, <https://www.python.org/>

- Ribas, Á., Bouy, H., & Merín, B. 2015, *A&A*, 576, A52
- Rieke, G. H., Young, E. T., Engelbracht, C. W., et al. 2004, *The Astrophysical Journal Supplement Series*, 154, 25
- Schmid, H. M., Joos, F., & Tschan, D. 2006, *A&A*, 452, 657
- Schneider, G., Grady, C. A., Hines, D. C., et al. 2014, *AJ*, 148, 59
- Smith, B. A. & Terrile, R. J. 1984, *Science*, 226, 1421
- Sommer, R. 2005, *ApJ*, 618, L161
- Sommer, R., Pueyo, L., & Larkin, J. 2012, *ApJ*, 755, L28
- Stolker, T., Bonse, M. J., Quanz, S. P., et al. 2019, *A&A*, 621, A59
- Stolker, T., Dominik, C., Avenhaus, H., et al. 2016, *A&A*, 595, A113
- Strom, K. M., Strom, S. E., Edwards, S., Cabrit, S., & Skrutskie, M. F. 1989, *AJ*, 97, 1451
- Tetzlaff, N., Neuhäuser, R., & Hohle, M. M. 2011, *MNRAS*, 410, 190
- Tilling, I., Woitke, P., Meeus, G., et al. 2012, *A&A*, 538, A20
- Van der Walt, S., Schönberger, J. L., Nunez-Iglesias, J., et al. 2014, *PeerJ*, 2, e453
- Varosi, F. & Gezari, D. Y. 1993, in *Astronomical Data Analysis Software and Systems II*, Vol. 52, 393
- Vigan, A., Moutou, C., Langlois, M., et al. 2010, *MNRAS*, 407, 71
- Wenger, M., Ochsenbein, F., Egret, D., et al. 2000, *A&AS*, 143, 9
- Werner, M. W., Roellig, T. L., Low, F. J., et al. 2004, *The Astrophysical Journal Supplement Series*, 154, 1
- White, R. J. & Basri, G. 2003, *ApJ*, 582, 1109
- Wolff, S. G., Perrin, M., Millar-Blanchaer, M. A., et al. 2016, *ApJ*, 818, L15
- Wray, J. D. 1966, *AJ*, 71, 403
- Wyatt, M. C., Dent, W. R. F., & Greaves, J. S. 2003, *MNRAS*, 342, 876
- Wyatt, M. C., Panić, O., Kennedy, G. M., & Matrà, L. 2015, *Ap&SS*, 357, 103

Appendix A: Reference star library

To remove both stellar halo and instrumental artifacts in the data on Wray 15-788 obtained with SPHERE in CI mode, we made use of an approach based on RDI in combination with PCA. The stars used for our reference library are all young, K-type star members of LCC subgroup of Sco-Cen. We list the names and corresponding observational parameters in Table A.1. We observed 26 and 12 reference stars (PI: M. A. Kenworthy) in H - and K_s -band, respectively. The same observational setup as for the science data on Wray 15-788 was used.

Appendix B: Other reduction strategies

In addition to the results presented in section 4, we apply other data reduction strategies for both SPHERE/CI and SPHERE/DPI data. That way, we want to test the stability of the detected disk's appearance and morphology.

Appendix B.1: CI data

Fig. B.1 shows the individual analysis of the dataset on Wray 15-788. We do not subtract any PSF model, but only de-rotate the images to have north pointing up and east towards the left. The median combined image of the four exposures is presented. In frames **a** and **b** we show this result for H and K_s -band, respectively. Whereas there is no obvious detection of the disk in H -band, the outer ring and the gap are marginally visible in the K_s -band result. Furthermore, the brightness asymmetry from northwest towards the southeastern part can marginally be recovered as well. To obtain the results presented in frames **c** and **d** of Fig. B.1, we additionally apply an unsharp mask to the results from the top panel of the figure. For unsharp masking, we use a Gaussian kernel with a FWHM of the instrumental PSF size of 50 mas and 55 mas in H -band and in K_s -band, respectively. Due to this high-pass filtering we are able to detect some structures of the outer ring in both filters. Furthermore, the gap of the disk is highlighted.

Appendix B.2: DPI data

In addition to the linear Stokes parameters Q and U , we derive their azimuthal analogs Q_ϕ and U_ϕ according to Schmid et al. (2006) as

$$Q_\phi = Q \cos(2\phi) + U \sin(2\phi) \quad (\text{B.1})$$

$$U_\phi = Q \sin(2\phi) - U \cos(2\phi), \quad (\text{B.2})$$

where ϕ denotes the position angle as defined before. By construction, $Q_\phi > 0$ refers to a polarization direction azimuthally oriented around the star. This is what we expect from stellar flux being recorded on the detector after a single scattering event at the dust grains of the disk. A negative value of Q_ϕ , however, represents a polarization vector radially aligned to the star. The U_ϕ image can be used as a measure of an upper limit on the noise inside the Q_ϕ frame.

We present the azimuthal Stokes vectors in Fig. B.2. The images are smoothed with a Gaussian kernel having a FWHM of the PSF size and are scaled with the squared radial distance to the image center. Both frames are normalized to the minimum and maximum value of the Q_ϕ image.

In the Q_ϕ image, we detect a clear indication of azimuthally polarized flux south-east of the star. This agrees very well with

our other observations from section 4. However, due to the non-optimal observing conditions the noise level is rather high, as seen in the U_ϕ frame. Therefore, the data is not suited to study the morphology of the disk or to quantitatively compare it to the CI results presented in the top panel of Fig. 1.

Table A.1. Observations of reference stars carried out with SPHERE/IRDIS. All data were obtained in classical imaging mode.

| Target (2MASS ID) | Observation date (yyyy-mm-dd) | Filter ^(a) | NDIT×DIT ^b (1×s) | $\langle\omega\rangle^d$ ($''$) | $\langle X\rangle^e$ | $\langle\tau_0\rangle^f$ (ms) |
|----------------------|----------------------------------|-----------------------|--------------------------------|--------------------------------------|----------------------|----------------------------------|
| J11272881-3952572 | 2017-04-18 | <i>H</i> | 4×32 | 1.51 | 1.10 | 1.40 |
| J11320835-5803199 | 2017-06-17 | <i>H</i> | 4×32 | 0.67 | 1.47 | 2.90 |
| J11445217-6438548 | 2018-05-14 | <i>H</i> | 4×32 | 0.73 | 1.31 | 2.38 |
| J11445217-6438548 | 2018-05-14 | <i>K_s</i> | 4×32 | 0.78 | 1.31 | 2.60 |
| J12065276-5044463 | 2017-04-02 | <i>H</i> | 3×32 | 1.24 | 1.12 | 1.50 |
| J12090225-5120410 | 2018-05-15 | <i>H</i> | 4×32 | 0.86 | 1.12 | 2.70 |
| J12090225-5120410 | 2018-05-15 | <i>K_s</i> | 4×32 | 0.70 | 1.12 | 2.90 |
| J12101065-4855476 | 2017-04-18 | <i>H</i> | 4×32 | 1.71 | 1.15 | 1.40 |
| J12123577-5520273 | 2017-06-17 | <i>H</i> | 4×32 | 0.77 | 2.41 | 2.80 |
| J12185802-5737191 | 2017-06-17 | <i>H</i> | 2×32 | 0.72 | 1.22 | 2.70 |
| J12220430-4841248 | 2017-04-18 | <i>H</i> | 3×32 | 1.82 | 1.17 | 1.40 |
| J12234012-5616325 | 2017-06-17 | <i>H</i> | 4×32 | 0.63 | 1.73 | 3.45 |
| J12393796-5731406 | 2017-06-17 | <i>H</i> | 4×32 | 0.64 | 1.77 | 3.83 |
| J12404664-5211046 | 2018-04-30 | <i>H</i> | 4×32 | 0.75 | 1.13 | 7.05 |
| J12404664-5211046 | 2018-04-30 | <i>K_s</i> | 4×32 | 0.87 | 1.13 | 7.10 |
| J12454884-5410583 | 2018-04-30 | <i>H</i> | 4×32 | 0.71 | 1.15 | 6.93 |
| J12454884-5410583 | 2018-04-30 | <i>K_s</i> | 4×32 | 0.66 | 1.15 | 8.98 |
| J12480778-4439167 | 2017-06-17 | <i>H</i> | 4×32 | 0.90 | 1.34 | 2.75 |
| J13055087-5304181 | 2018-07-04 | <i>H</i> | 4×32 | 0.82 | 1.14 | 1.95 |
| J13055087-5304181 | 2018-07-04 | <i>K_s</i> | 4×32 | 0.93 | 1.14 | 2.03 |
| J13064012-5159386 | 2018-04-30 | <i>H</i> | 4×32 | 0.56 | 1.13 | 8.15 |
| J13064012-5159386 | 2018-04-30 | <i>K_s</i> | 4×32 | 0.56 | 1.13 | 9.88 |
| J13065439-4541313 | 2018-04-08 | <i>H</i> | 4×32 | 0.46 | 1.09 | 5.65 |
| J13065439-4541313 | 2018-04-08 | <i>K_s</i> | 4×32 | 0.55 | 1.09 | 4.68 |
| J13095880-4527388 | 2018-05-01 | <i>H</i> | 4×32 | 1.08 | 1.07 | 2.70 |
| J13095880-4527388 | 2018-05-01 | <i>K_s</i> | 4×32 | 1.03 | 1.07 | 2.45 |
| J13103245-4817036 | 2018-05-01 | <i>H</i> | 4×32 | 1.03 | 1.10 | 3.30 |
| J13103245-4817036 | 2018-05-01 | <i>K_s</i> | 4×32 | 0.87 | 1.10 | 4.40 |
| J13121764-5508258 | 2018-05-15 | <i>H</i> | 4×32 | 0.62 | 1.16 | 2.50 |
| J13121764-5508258 | 2018-05-15 | <i>K_s</i> | 4×32 | 0.62 | 1.16 | 3.00 |
| J13174687-4456534 | 2018-05-28 | <i>H</i> | 4×32 | 0.70 | 1.07 | 4.33 |
| J13174687-4456534 | 2018-05-28 | <i>K_s</i> | 4×32 | 0.67 | 1.07 | 4.15 |
| J13233587-4718467 | 2017-04-02 | <i>H</i> | 4×32 | 1.68 | 1.21 | 1.40 |
| J13334410-6359345 | 2017-07-05 | <i>H</i> | 4×32 | 1.06 | 1.53 | 3.05 |
| J13354082-4818124 | 2017-04-02 | <i>H</i> | 4×32 | 1.06 | 1.30 | 2.08 |
| J13380596-4344564 | 2017-04-02 | <i>H</i> | 4×32 | 1.05 | 1.33 | 2.40 |
| J13455599-5222255 | 2018-04-28 | <i>H</i> | 4×32 | 0.64 | 1.13 | 6.35 |
| J13455599-5222255 | 2018-04-28 | <i>K_s</i> | 4×32 | 0.65 | 1.13 | 6.03 |

Notes. ^(a) A broadband filter in either *H*- or *K_s*-band was applied. ^(b) NDIT describes the number of dithering positions and DIT is the detector integration time per dithering position. ^(c) $\Delta\pi$ describes the amount of field rotation during the observation, if it is carried out in pupil-stabilized mode (only valid for CI observations). ^(d) $\langle\omega\rangle$ denotes the average seeing conditions during the observation. ^(e) $\langle X\rangle$ denotes the average airmass during the observation. ^(f) $\langle\tau_0\rangle$ denotes the average coherence time during the observation.

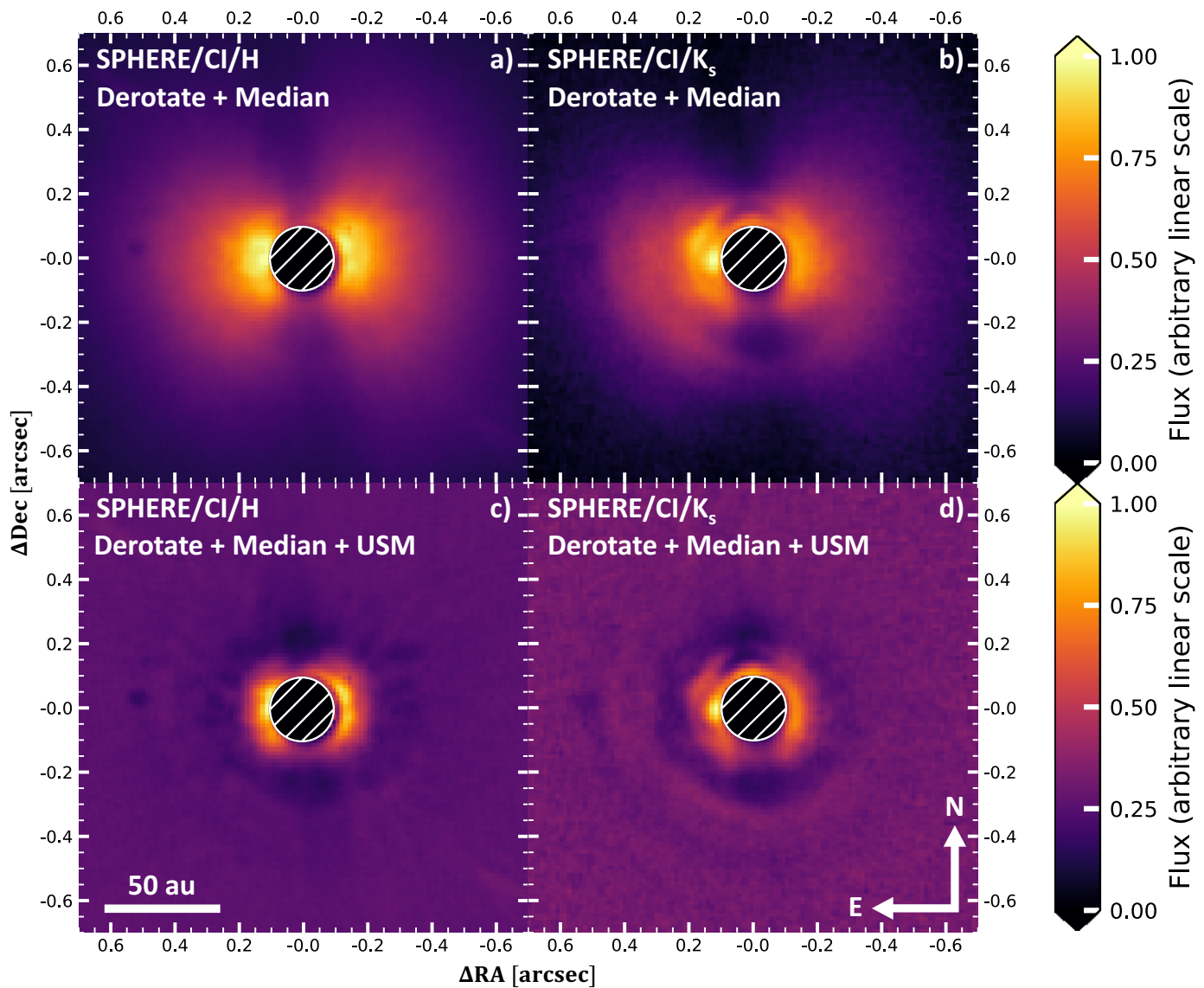


Fig. B.1. Other reductions of SPHERE classical imaging data on WRAY 15-788. The images are normalized to the maximum in each frame and arbitrarily, linearly scaled. No subtraction of the stellar point-spread function (PSF) is performed. For all images north is up and east is left. Images **a** and **b** show the de-rotated and median combined image stack of science frames in H - and K_s -band, respectively. Frames **c** and **d** represent the same image as above, but an additional unsharp mask (USM) is applied (Gaussian kernel with full width at half maximum equal PSF size).

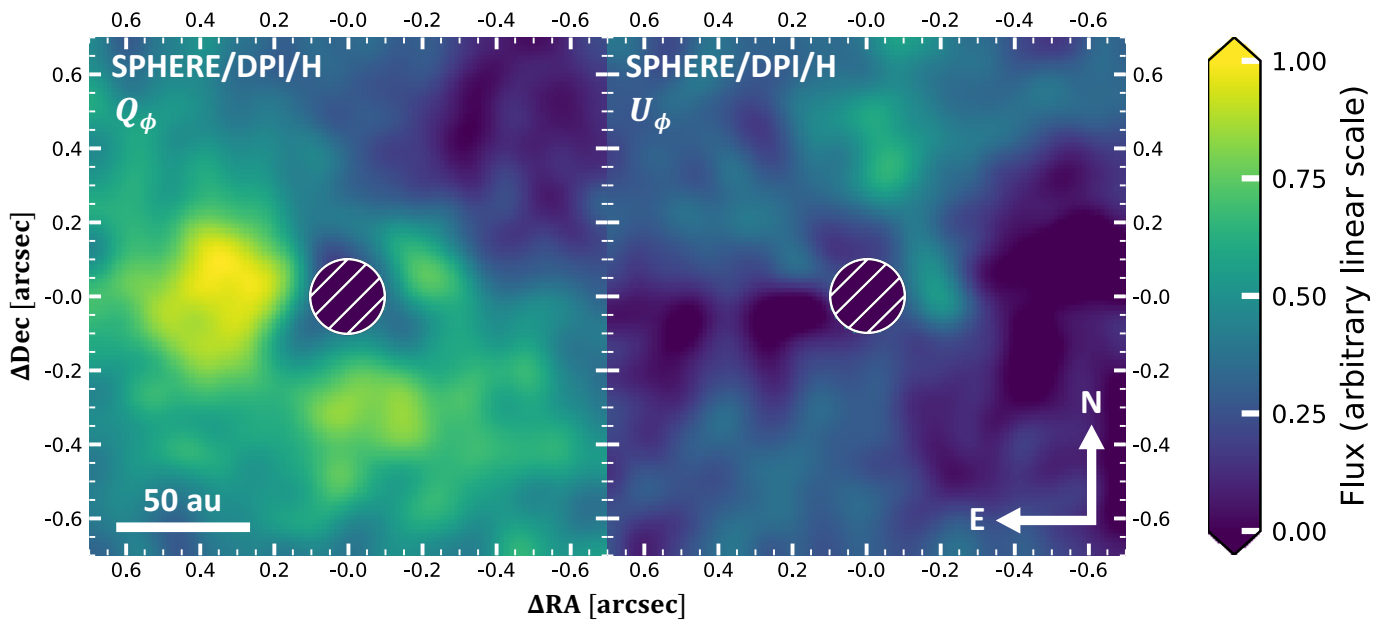


Fig. B.2. Other reductions of SPHERE dual-polarimetric imaging data on WRAY 15-788. We present the azimuthal Stokes parameters Q_ϕ and U_ϕ within the left and right panel, respectively. Both images are scaled with r^2 and normalized with respect to the minimum and maximum flux in the Q_ϕ frame. In both frames north is up and east is left.